Carbonaceous biosignatures of diverse chemotrophic microbial communities from chert nodules of the Ediacaran Doushantuo Formation

Yuangao Qu [a,b,*], Jiasheng Wang [c], Shuhai Xiao [d], Martin Whitehouse [b], Anders Engdahl [e], Guangzhe Wang [c], Nicola McLoughlin [f,g]

[a] Centre for Geobiology, University of Bergen, Norway
[b] Swedish Museum of Natural History, Sweden
[c] State Key Laboratory of Biogeology and Environmental Geology, School of Earth Sciences, China University of Geosciences (Wuhan), China
[d] Department of Geosciences, Virginia Tech, USA
[e] MAX IV Laboratory, Lund University, Sweden
[f] Department of Geology, Rhodes University, South Africa
[g] Albany Museum, Grahamstown, South Africa

ARTICLE INFO

ABSTRACT

The Ediacaran Doushantuo Formation (DST) is renowned for exceptionally preserved Precambrian fossils including metazoans. Some of these fossils, particularly microfossils such as multicellular algae and acanthomorphic acritarchs, are preserved in DST chert nodules. To better understand the geomicrobiological processes that contributed to the authigenic formation of DST chert nodules and facilitated exceptional fossil preservation, we analyzed organic matter in these chert nodules and the surrounding matrix (calcareous mudstone) using multiple in-situ techniques: confocal laser Raman spectroscopy, micro-Fourier transform infrared spectroscopy (FTIR), and secondary ion mass spectroscopy (SIMS). We found strong ultrastructural, chemical, and isotopic heterogeneities in the organic matter as indicated by the Raman spectral parameter I-1350/1600 ranging from 0.49 to 0.88, the infrared spectral index $R_{3/2}$ from 0.12 to 0.90, and an estimated $\delta13C_{org\text{-}SIMS}$ range of 44‰ (V-PDB). These micron-scale heterogeneities imply that the organic matter preserved in the DST chert nodules is derived from different carbonaceous sources in a diverse microbial ecosystem, including eukaryotic and/or prokaryotic photoautotrophs, as well as chemotrophs involved in the fermentation and probably anaerobic oxidation of organic remains. Thus, the microbial ecosystems in Ediacaran ocean waters and sediments were more complex than previously thought, and these microbial processes controlled dynamic micro-environments in DST sediments where chert nodules were formed and fossils were mineralized. The results also show that variations in the relative abundances, activities, and interactions of co-existing microorganisms in DST sediments may have modulated $\delta13C_{org}$ shifts, causing local decoupling between $\delta13C_{org}$ and $\delta13C_{carb}$ as measured in bulk samples.

© 2017 Elsevier B.V. All rights reserved.

1. Introduction

The Ediacaran Doushantuo Formation (DST) of South China preserves an exceptional geological record to help decode the co-evolution of life and the Earth system during the Proterozoic-Phanerozoic transition (Xiao et al., 2014a). Highly diverse fossils have been reported in the DST, including possible metazoan embryos (Xiao et al., 1998, 2007; Chen et al., 2004, 2009; Hagadorn et al., 2006; Yin et al., 2007), cyanobacteria, sulfur bacteria, multicellular algae, and acanthomorphic acritarchs (Xiao, 2004; Xiao et al., 2014b; McFadden et al., 2008, 2009; Bailey et al., 2013). The litho-, bio- and chemo-stratigraphy of the DST has been well characterized with a detailed record of lithological variations, the distribution of fossil groups, profiles of Fe speciation and isotope of $\delta^{13}C$, $\delta^{34}S$, $\delta^{56}Fe$ (e.g., Guo et al., 2006; McFadden et al., 2008; Jiang et al., 2010, 2012; Li et al., 2010; Xiao et al., 2012; Fan et al., 2014).

The DST was deposited on a passive continental margin of the Yangtze Craton (Li et al., 2010; Jiang et al., 2011). The age of the

---

* Corresponding author at: Centre for Geobiology, University of Bergen, Norway.
E-mail address: qu_yuangao@hotmail.com (Y. Qu).

DST is constrained between 635.2 ± 0.6 Ma and 551.1 ± 0.7 Ma on the basis of U-Pb dates of zircons in volcanic ash beds and re-Os geochronology of black shales (Condon et al., 2005; Liu et al., 2009; Zhu et al., 2013). The formation is widely distributed in South China with a number of different sections across depositional environments from the inner shelf (e.g. Baokang, and Chadian sections), shelf lagoon (e.g. Jiulongwan section), outer shelf (e.g. Weng'an section), slope (e.g. Tianping and Siduping sections), to oceanic basin (e.g. Wuhe and Longe sections, see Muscente et al. (2015) for a comprehensive summary).

The Jiulongwan section in the Yangtze Gorges area (Fig. 1A) preserves a well exposed succession of the DST and has been studied extensively (e.g., McFadden et al., 2008). At the Jiulongwan and other sections in the Yangtze Gorges area, abundant microfossils have been discovered from chert nodules (Fig. 1B; Yin et al., 2004; McFadden et al., 2008; Xiao et al., 2010; Shen et al., 2011; Muscente et al., 2015). These chert nodules are authigenic or early diagenetic in origin and were formed below the water-sediment interface in an anoxic-euxinic shelf lagoon (Xiao et al., 2010; Shen et al., 2011). They typically contain decayed microbial organic matter and fragments of microbial mats in the siliceous center or core that is surrounded by an inner rim of pyrite and an outer rim of blocky calcite (see Fig. 2 in Xiao et al., 2010). Silica sources for chert nodule formation likely came from seawaters and clay diagenesis rather than hydrothermal vents based on silicon isotopes, REE patterns, and Ge/Si ratios (Shen et al., 2011; Wen et al., 2016). Highly positive pyrite $\delta^{34}S$ values (15.2–29.8‰ VCDT) and small sulfur isotopic fractionation (<22‰) between pyrite and carbonate associated sulfate (CAS) measured on these chert nodules indicate rapid bacterial sulfate reduction (Xiao et al., 2010). It was proposed that bacterial sulfate reduction induced pyrite precipitation and decreased pH in the pore water, causing carbonate dissolution and silica precipitation just beneath the sediment water interface and underneath anoxic seawaters with low SO_4^{2-}, high Fe^{2+}, and high H_4SiO_4 concentrations (Xiao et al., 2010). However, it is possible that other microbial processes of chemotrophy, such as fermentation, methanogenesis, and methanotrophy could also be involved in the degradation of organic carbon and played a role in chert nodule formation and hence fossil silicification.

In order to shed light on the complex microbial processes involved in the authigenic formation of DST chert nodules, we analyzed these nodules using a combination of in-situ techniques to characterize organic matter in chert nodules and their host rocks in the lower Member II of the DST at the Jiulongwan section in the Yangtze Gorges area, South China. The objectives are: 1) to study the μm-scale structural, chemical, and isotopic heterogeneities of organic matter in the chert nodules in order to identify primary biosignatures of co-existing microbial communities and processes; 2) to assess the taphonomic effects of these microbial processes on the organic matter preserved in the chert nodules; 3) to understand the origin of $\delta^{13}C_{org}$ heterogeneity and its impact on our views of the Ediacaran carbon cycle.
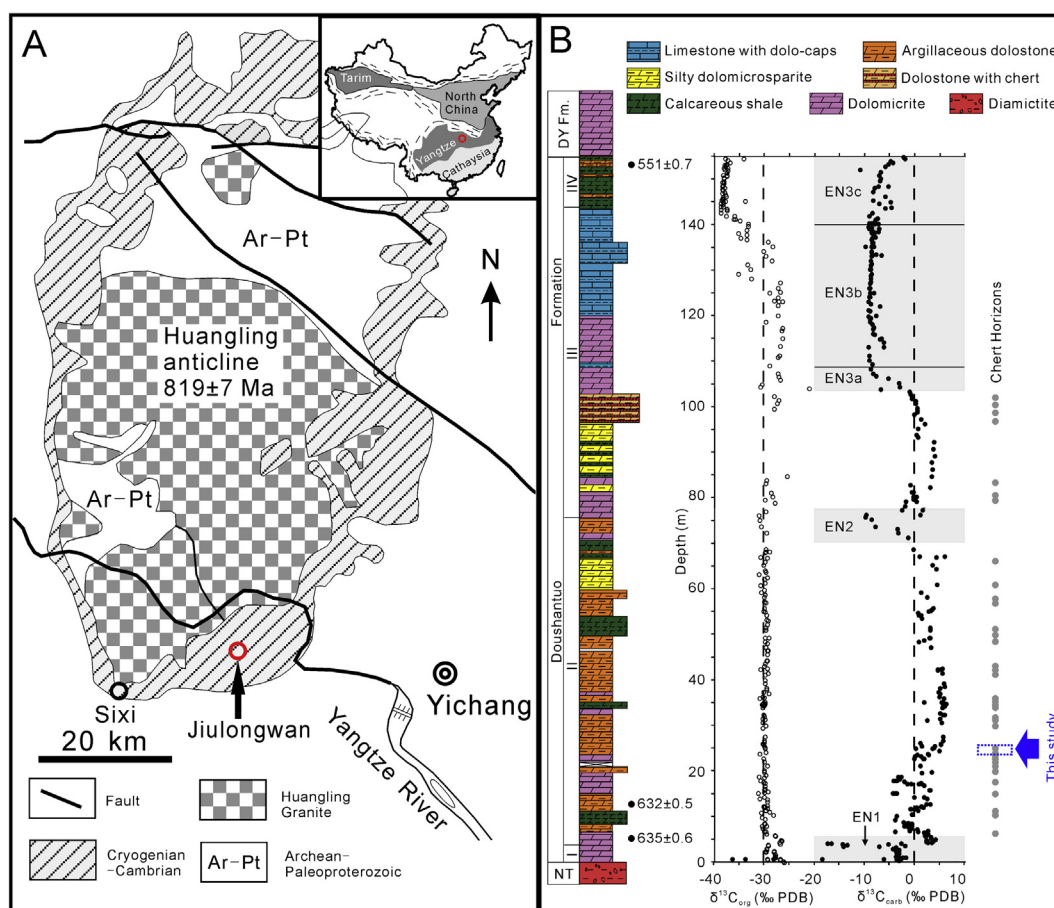
Fig. 1. Geological map and chemostratigraphy of the Doushantuo Formation at Jiulongwan section in the Yangtze Gorges area. (A) Simplified geological map with geographic location of Jiulongwan section (red cycle). Modified from Xiao et al. (2010). (B) Stratigraphic column of the Doushantuo Formation with $\delta^{13}C_{org}$ and $\delta^{13}C_{carb}$ profiles after McFadden et al. (2008). Radiometric ages are from Condon et al. (2005). The distribution of chert nodules (gray dots) is from Xiao et al. (2010) and Shen et al. (2011). Blue box shows the stratigraphic interval where chert nodules studied here were collected. (For interpretation of the references to colour in this figure legend, the reader is referred to the web version of this article.)

2. Geological setting and samples

The DST at the Jiulongwan section, located southeast of Zigui Town in the Yangtze Gorges area (Fig. 1A), is approximately 155 m thick and consists of a mixture of carbonates and shales. The DST can be subdivided into four stratigraphic members. Member I is an interval of c. 5 m-thick ^{13}C-depleted dolostone (e.g., the cap carbonate) overlying Cryogenian diamictite of the Nantuo Formation (Fig. 1B). Member II consists of c. 70 m-thick dolostones interbedded with black shales, and contains abundant cm-size chert nodules with exceptionally preserved microfossils (Liu et al., 2014; Mcfadden et al., 2008, 2009; Xiao, 2004; Xiao et al., 2010; Shen et al., 2011). Member III is ~65 m in thickness, consisting of dolostone in the lower part and intercalated dolostone and limestone in the upper part. Member IV is a unit of c. 10 m thick black shales with dm- and cm-sized carbonate concretions.

Carbon isotope chemostratigraphy of the DST at Jiulongwan and nearby sections has been characterized in several previous studies (Zhou and Xiao, 2007; Jiang et al., 2007; McFadden et al., 2008; Tahata et al., 2013). $\delta^{13}C_{carb}$ shows a negative excursion (EN1 in Fig. 1B) in the cap carbonate (Member I), followed by rapid variations between positive and negative values in lower Member II, and the predominantly positive values in the rest of Member II. $\delta^{13}C_{carb}$ then decreases to negative values (EN2 in Fig. 1B) near the boundary between Member II and III, succeeded by positive values in the lower Member III and a prominent negative excursion down to $-10‰$ in the upper Member III and Member IV (EN3 in Fig. 1B, widely accepted as equivalent to the Shuram excursion; Grotzinger et al., 2011). $\delta^{13}C_{org}$ values, on the other hand, are nearly constant around $-29‰$ in Member II, and increase to slightly higher values in Member III before plunging to $-39‰$ in Member IV Fig. 1B).

Chert nodules first appear near the base of Member II, where $\delta^{13}C_{carb}$ values begin to increase to c. 4‰ from negative values in the underlying 'cap carbonate' of Member I (Fig. 1B), and become more abundant but transition to chert lenses and bands in the overlying strata of lower Member III (Fig. 1B; McFadden et al., 2008). Chert nodules analyzed in this study were collected from lower Member II of the DST, about 25 m above the Doushantuo-Nantuo boundary, at the Jiulongwan section (Fig. 1B). Ten polished thin sections with a thickness of approximately 40 μm were made for petrography and Raman spectroscopic analyses. Two doubly polished rock wafers of c. 25 μm thick were prepared for the micro-FTIR analysis. Two polished thin sections of c. 40 μm thick were selected for SIMS analysis.

3. Methods

3.1. Microscopy and Raman spectroscopy

Raman spectroscopy is a useful tool for analyzing the structural order of carbonaceous material, because different modes of bond vibration from various molecular structures (e.g. hexagonal ring, heteroatoms, dangling bonds, tetrahedral coordinated carbons, and aromatic substances) give rise to specific bands in the Raman spectra (Tuinstra and Koenig, 1970; Beyssac et al., 2002; Sadezky et al., 2005; Lahfid et al., 2010; Kouketsu et al., 2014; Romero-Sarmiento et al., 2014). In particular, two-dimensional Raman mapping is an efficient technique to quantify the μm-scale ultrastructural heterogeneities of organic matter within individual microfossils (Foucher et al., 2015; Qu et al., 2015), recording different compounds from co-existing organisms (e.g. plants, fungi, cyanobacteria).

In this study, we employed Raman spectroscopy to assess the ultrastructural characteristics of organic matter within DST chert nodules, and to infer the co-existing microorganisms and microbial processes by identifying μm-scale structural heterogeneities. Highly polished thin sections were made for both petrographic and Raman spectroscopic analyses. Raman analysis was conducted in the Centre for Geobiology at University of Bergen. A Horiba-Jobin Labram 800 HR Raman spectrometer linked to an Olympus BX41 petrographic microscope was used in Raman spectroscopic analysis. The Raman spectra were acquired using a 514 nm Ar-ion laser with absolute laser power of 15–20 mW through a density filter (D = 0.3), an aperture hole of 100 μm in diameter, and a $100 \times$ objective with a final power of c. 2.5 mW in a 1–2 μm spot on the sample (measured with a Coherent Lasercheck Analyser). The laser beam was focused on the carbonaceous material underneath the polished surface of thin sections in order to avoid surface contamination and polishing artifacts (Beyssac et al., 2003; Ammar and Rouzaud, 2012). The Raman spectra were obtained in the range of 150–2000 cm^{-1} with the acquisition time of 2×10 s. Some targeted areas were scanned on an XY stage with a spatial resolution of 1 μm per step in order to obtain data sets for generating two-dimensional maps of Raman spectral parameters. The spectra were processed with the software "Lab Spec version 5.58.25".

3.2. Micro-FTIR

Micro-FTIR can be used to investigate the chemical composition of organic matter in fossils and rocks using the IR spectral bands characteristic of various vibrations of functional groups on the carbon chain, such as the stretching and bending vibrations of bonds of C—H, C—N, C=O, C—O in aliphatic and aromatic molecules (e.g. Marshall et al., 2005; Igisu et al., 2006, 2009, 2014). The absorbance ratio of asymmetric stretching band of aliphatic CH$_3$ end-methyl versus CH$_2$ chain-methylene describes the branching index of carbon chains. This ratio is defined as $R_{3/2}$ = intensity ratio of 2960 cm^{-1}-band/2925 cm^{-1}-band, and it has been used to describe the branching index of carbon chains in fossilized carbonaceous material (Igisu et al., 2006, 2009; Qu et al., 2015). It has been proposed that the $R_{3/2}$ ratio shows systematic variations between biomass of archaeans, bacteria, and eukaryotes due to their different chemical compositions within cellular constituents, especially the membrane lipids (Igisu et al., 2009). It has also been demonstrated that different subcellular components (e.g. cell wall and protoplasm) in a single cell may have different $R_{3/2}$ ratios (Qu et al., 2015).

In this study, micro-FTIR was used to investigate the μm-scale heterogeneities of organic matter $R_{3/2}$ in DST chert nodules. The in-situ infrared analysis was performed on doubly polished rock wafers using an infrared microscope coupled to an infrared spectrometer in transmission mode at Beamline D7 in the MAX III ring of Maxlab in Lund, Sweden. The FTIR equipment consists of a Bruker IFS66V FTIR spectrometer, a Bruker Hyperion 3000 microscope with a $15\times$ IR objective, and a 100×100 μm MCT detector for the mid infrared region. An aperture was used to focus on the target fossils and carbonaceous material, with measured spot size of 15×15 μm^2. The rock wafer samples were placed on a CaF$_2$ window and infrared spectra were acquired. A reference background IR spectrum was measured on the CaF$_2$ window before the measurement of every sample. The spectra were acquired from wavenumber 500 to 7500 cm^{-1} by the integration of 256 scans, and were represented as IR absorbance in this range. The IR spectra were processed using the software Lab Spec version 5.58.25.

3.3. Secondary ion mass spectrometry (SIMS)

Carbon isotopic fractionation is imparted by biological processes when organisms preferentially assimilate ^{12}C in the carbon source due to kinetic effects. The carbon isotopic composition of

the resulting biomass is controlled by the composition of the carbon source (e.g. CO_2, dissolved inorganic carbon-DIC, CH_4, acetate) and the metabolic pathway (e.g. phototropy, chemotrophy) of assimilation (House et al., 2003; Zerkle et al., 2005). Thus the carbon isotopic compositions of organic matter and carbonate preserved in sedimentary rocks can be used to infer biological processes and the carbon cycle in geological past (e.g. Schidlowski, 2001). Recent technological advances have made it possible to measure in-situ carbon isotopic compositions of individual microfossils using secondary ion mass spectrometry (SIMS), which enables direct correlation between fossil morphologies and isotopic compositions, and this approach has been particularly insightful for studying Precambrian microfossils and metabolic pathways (Kaufman and Xiao, 2003; Williford et al., 2013; Lepot et al., 2013; House et al., 2013).

In this study, we used SIMS to investigate the μm-scale carbon isotopic characteristics of organic matter in DST nodules with the goal of distinguishing the different microbial components and their metabolic pathways that affected chert nodule formation and fossil preservation. The in-situ carbon isotopic analysis of organic matter was performed using a Cameca IMS 1280 at the NordSIM-facility in the Swedish Museum of Natural History in Stockholm. To prepare samples for SIMS analysis, a sector of the sample was cut from a polished disc and mounted together with the graphite standard of pyrolytic graphite ('C-pyr' which has $\delta^{13}C_{V-PDB}$ = −31‰; G. D. Layne, personal communication). The samples were coated with a c. 30 nm gold layer to provide conductivity. Analytical methods for determination of carbon isotope ratios closely follow those for calcite described by Drake et al. (2015). Briefly, a 20 kV impact energy Cs^+ beam was focused to a 5–10 μm spot, and a low energy
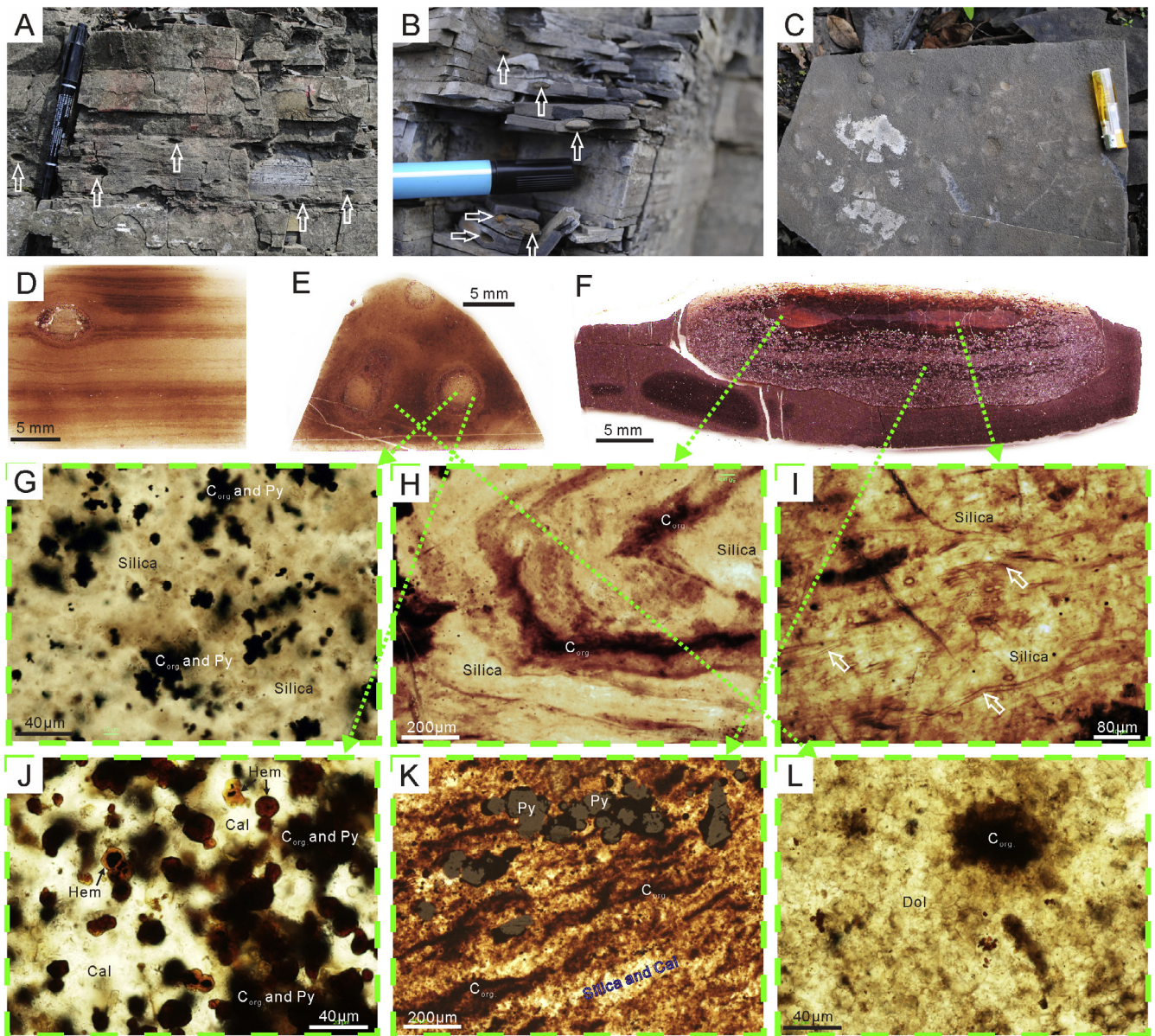
Fig. 2. Outcrop and petrographic features of DST chert nodules. (A)–(C) Occurrence of chert nodules (white arrows) on freshly exposed outcrops and slabs. (D)–(F) Overview of chert nodules in thin sections cut perpendicular to (D and F) and parallel to (E) bedding surfaces. (G)–(L) Optical microscopic images of (E–F), with green arrows denoting areas of magnification. (G) Organic matter and pyrite in silica matrix in nodule center. (H) Organic laminae in silica matrix in nodule center. (I) Filamentous microfossils (white arrows) in silica matrix in nodule center. (J) Organic particles, pyrite and occasional hematite crystals in calcite matrix in nodule rim. (K) Microbial mat fragments and pyrite crystals in silica matrix in nodule rim. (L) Organic matter in dolomitic matrix of host rock. Abbreviations: C_{org} = organic matter; Cal = calcite; Dol = dolomite; Py = pyrite; Hem = hematite. (For interpretation of the references to colour in this figure legend, the reader is referred to the web version of this article.)

electron flooding gun was used to compensate for charge build-up. Measurements were made in high transmission transfer mode with simultaneous determination of the ^{12}C and ^{13}C signals in a Faraday cup and low-noise ion counting electron multiplier, respectively, the latter of which was operated at high mass resolution (M/DM ~3000) to separate $^{13}C^-$ from $^{12}C^1H^-$. Carbon isotopic data were calibrated using the graphite standard and are reported as ‰ deviation from V-PDB. Given that the carbonaceous material in the samples experienced little metamorphism and thus has lower structural order than the graphite standard, there is some uncertainty in isotopic calibration using a graphite standard (Williford et al., 2013). Hence, in our discussion and interpretation, we focus more on $\delta^{13}C$ ranges and spatial heterogeneities, rather than absolute $\delta^{13}C$ values.

4. Results

4.1. Petrography of DST chert nodules

The chert nodules in the lower Member II are mm- to cm-sized spheroidal and ellipsoidal structures (Figs. 2A–C). The host rocks are thin-bedded dolostones, argillaceous dolostones, mudstones, and shales (Figs. 2A–C). In thin sections, the long-axis of the chert nodules are oriented parallel to micro-laminae in the host rock, and these laminae tend to bend around the chert nodules (Figs. 2D), suggesting that the nodules were formed during early diagenesis before sediment compaction.

The nodules contains clotted organic particles, discontinuous organic laminae interpreted as chips of microbial mats, and larger mat fragments with filamentous microfossils in the microcrystalline quartz matrix of the nodule center (Figs. 2G–I). The rim of the nodules consists of clotted organic particles, discontinuous organic laminae, euhedral pyrite crystals and occasionally hematite in the mineral matrix of microcrystalline quartz and micritic calcite (Figs. 2J and K). The discontinuous organic laminae and traces of pyrite minerals are oriented more or less parallel to the bedding of the host rock (Fig. 2K). Some organic particles can also be seen in the host rock (Fig. 2L).

4.2. Raman spectroscopy and the structural order of organic matter

All Raman spectra show the typical features of disordered carbonaceous material with two broad bands at around 1350 and 1600 cm^{-1} (Fig. 3). The organic matter in the center of the nodules also shows a peak at 465 cm^{-1}, representing the existence of microcrystalline quartz or silica (Figs. 3A and B). Some Raman spectra of organic matter in the nodule rims have additional bands at 154, 281, 712 and 1086 cm^{-1} that are assigned to calcite (Fig. 3C), whereas others have a band at 465 cm^{-1} due to the presence of quartz (Fig. 3D). The bands at 176, 299 and 1096 cm^{-1} occur in the Raman spectra of organic matter in the host rock, indicating the existence of dolomite in the mineral matrix (Fig. 3E, Rividi et al., 2010). In order to remove the background fluorescence, spectra were subtracted by a linear baseline from 1000 to 1800 cm^{-1}, according to Kouketsu et al. (2014). In this study, we use the apparent intensity ratio of the band at 1350 vs. 1600 cm^{-1} (denoted as I-1350/1600, Fig. 3), which is commonly used to characterize the structural order of organic matter (e.g. Tuinstra and Koenig, 1970; Bonal et al., 2006; Foucher et al., 2015; Qu et al., 2015). In summary, the I-1350/1600 values of organic matter in nodule center, rim, and host rock vary across large ranges of 0.49–0.62, 0.51–0.71, and 0.49–0.88, respectively (Fig. 4A).

In order to further investigate these ultrastructural heterogeneities, two-dimensional Raman mappings were performed (Fig. 5). The intensities of the bands at 1350 cm^{-1} and 1600 cm^{-1}, defined as I-1350 and I-1600, respectively, record the abundance of the organic carbon (Fig. 5). The Raman spectral parameter I-1350/1600 reflects changes in the structural order of the organic matter. The I-1350 and I-1600 maps confirm petrographic observations, showing high concentrations of organic carbon in clotted organic particles, discontinuous organic laminae, and filamentous microfossils in the nodules center (Figs. 5A–D), rim (Fig. 5E) and host rock (Fig. 5F). The I-1350/1600 maps show strong spatial variations in the three fabric categories (Fig. 5), suggesting μm-scale ultrastructural heterogeneities.

4.3. Micro-FTIR and the branching index of carbon chain

All IR spectra obtained from the organic matter have distinct bands at 2850 cm^{-1}, assigned to the symmetric stretching vibration of C—H bond in CH$_2$ (Fig. 6). In addition, the bands at 2925 cm^{-1} and 2960 cm^{-1} are caused by the asymmetric stretching vibration of C—H bond in aliphatic CH$_2$ chain-methylene and CH$_3$ end-methyl, respectively (Fig. 6; Bellamy, 1954). The IR spectra from the organic matter in the center of the nodules contain seven bands at 1995, 1870, 1793, 1684, 1610, 1525, and 1492 cm^{-1} (Figs. 6A and B) derived from the overtones and combinations of Si-O vibrations in the siliceous mineral matrix (Ito and Nakashima, 2002). The broad bands in the range from 3700 to 3100 cm^{-1} (Fig. 6) correspond to the O—H stretching vibration of molecular H$_2$O (Aines and Rossman, 1984) that are probably derived from the mineral matrix. The IR spectra of the organic matter from the nodule rim and host rock have additional bands at 1820, 2525 and 2630 cm^{-1} (Figs. 6C–F) that are caused by the C—O vibrations (RRUFF data base), probably indicating the co-existence of carbonates in the mineral matrix.

The spectra in the range from 2800 to 3050 cm^{-1} were subtracted by a linear baseline to obtain the relative intensity of bands at 2960 and 2925 cm^{-1} (Fig. 6), according to Igisu et al. (2009, 2014). The intensity ratio of these two bands (I-2960 cm^{-1} vs. 2925 cm^{-1}, denoted as R$_{3/2}$) is a measure of the absorbance of the asymmetric stretching vibration of C—H in CH$_3$ vs. CH$_2$. This ratio can be used to characterize the branching index of carbon chains (Marshall et al., 2005; Igisu et al., 2009, 2014). The R$_{3/2}$ data are summarized and plotted in Fig. 4B, which again show large heterogeneities in branching index of organic matter in nodule center (0.12–0.73), nodule rim (0.43–0.90), and host rock (0.34–0.64), respectively.

4.4. $\delta^{13}C_{org-SIMS}$ measurements and variations in carbon isotopic compositions

The ^{12}C count rate obtained from the graphite standard was in the range of 8.4×10^7 to 6.6×10^7 cps (counts per second), whereas the organic matter in the chert nodules and host rocks yielded ^{12}C count rates between 2.7×10^7 and 5.6×10^3 cps (Supplementary information Table S1). The $\delta^{13}C_{org-SIMS}$ data with low count ratios arose from measurements with low concentrations of organic carbon and significant mineral matrix. There is a clear correlation between the calculated $\delta^{13}C_{org-SIMS}$ and the ^{12}C count rate when the ^{12}C count rate of the sample versus the standard is less than 3% (Supplementary information Fig. S1). We therefore exclude all data with count ratios less than 3% of the standard, and report only the relatively reliable $\delta^{13}C_{org-SIMS}$ data with count ratios greater than 3% (Supplementary information Fig. S1, Table S1).

The calculated $\delta^{13}C_{org-SIMS}$ values span a large range of c. 44‰ (Fig. 4C, Fig. 7), with the average values measured in the nodule rim and especially the center being more negatively shifted relative to the host rock. The range of $\delta^{13}C_{org-SIMS}$ values is −63.1 to
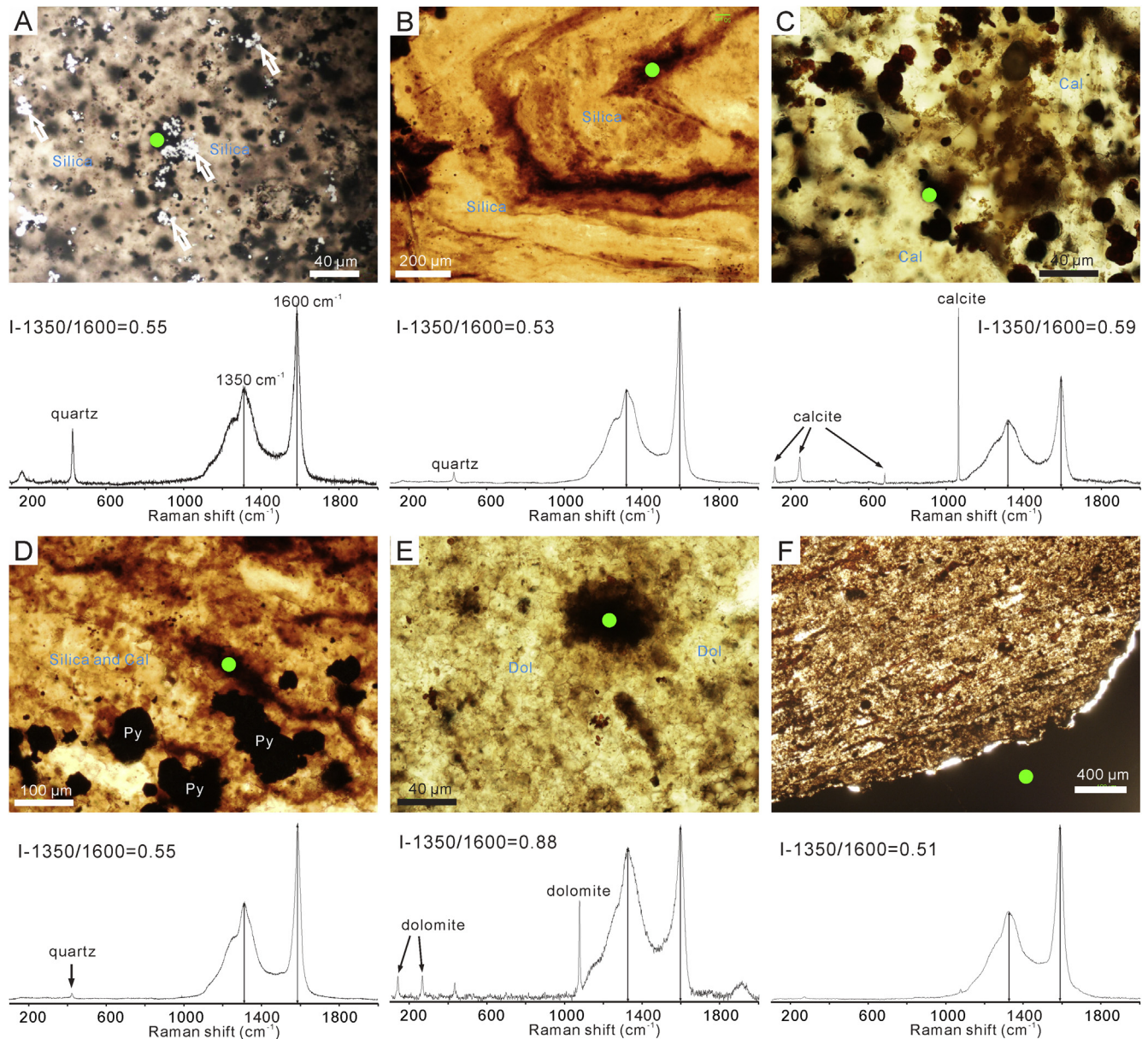
Fig. 3. Raman spectra of organic carbon in nodules with analyzed positions marked by green plots in corresponding petrographic images. (A) and (B) Organic matter and laminae in nodule center. Pyrite crystals are bright under reflecting light (arrows in A). (C) and (D) Organic particles (in C) and microbial mat fragments (in D) in nodule rim. (E) and (F) Organic matter in the dolomitic host rock. (For interpretation of the references to colour in this figure legend, the reader is referred to the web version of this article.)

−35.1‰, −56.7 to −25.9‰, and −54.8 to −18.5‰ for organic carbon in nodule center, rim, and host rock, respectively (Fig. 4C). These results show strong heterogeneities in organic carbon isotope compositions but an increasing trend of $\delta^{13}C_{org}$ from nodule center, nodule rim, to host rock.

5. Discussion

5.1. Raman spectroscopy and ultrastructural heterogeneities in organic matter

The structural order of organic matter in sedimentary rocks is controlled by the molecular structures of carbon precursors (Franklin, 1951; Bernard et al., 2010; Sforna et al., 2014; Qu et al., 2015) and influenced by secondary post-depositional processes including thermal alteration (Tuinstra and Koenig, 1970; Beyssac et al., 2002; Rahl et al., 2005; Schiffbauer et al., 2007, 2012; Kouketsu et al., 2014), deformation and shear force (Bustin et al., 1995; Aoya et al., 2010), hydrothermal fluid circulation and graphite deposition (Wopenka and Pasteris, 1993; Luque et al., 2009; Lepland et al., 2011; Galvez et al., 2013), and mineral-templating effect (van Zuilen et al., 2012).

In this study, the organic matter preserved in the chert nodules experienced the same peak-metamorphic temperature and geological history, and thus the I-1350/1600 values in each group (nodule center, rim and host rock) have similar mean values (Fig. 4A). Indeed, an analysis of variance (ANOVA) further suggests that there is no significant difference of measured I-1350/1600 among the three groups (p = 0.24, Fig. 4A). Consequently the ultrastructural heterogeneities of organic matter cannot be explained by different background peak-metamorphic temperatures and shear forces.
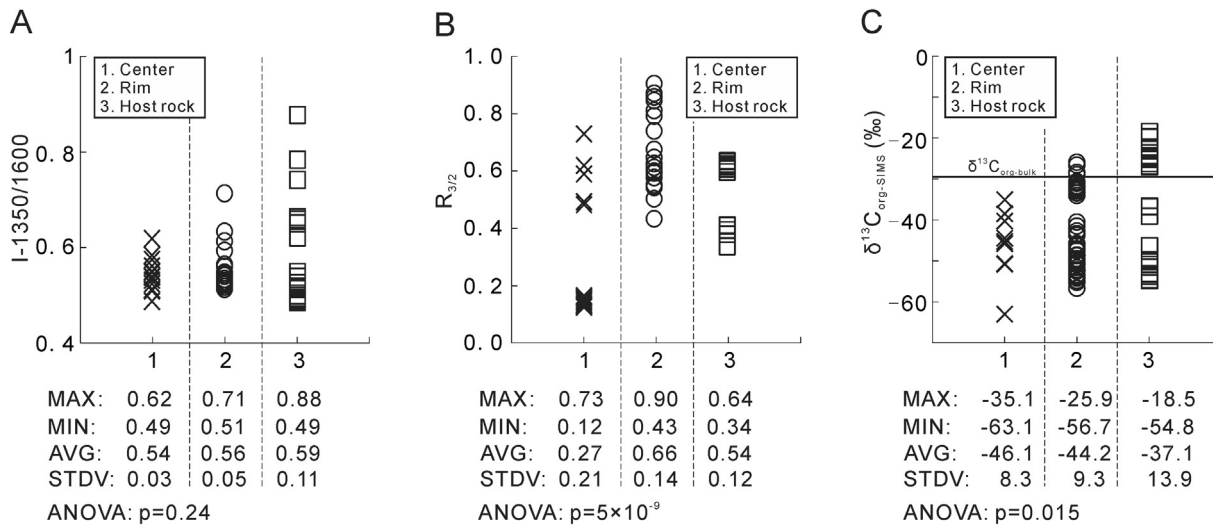
Fig. 4. Summary of plots showing variations in (A) Raman spectral parameter I-1350/1600, (B) $R_{3/2}$ branching index calculated from micro-FTIR spectra, and (C) $\delta^{13}C_{org\text{-}SIMS}$ of organic matter in nodule center, nodule rim, and host rock, respectively. $\delta^{13}C_{org\text{-}bulk}$ = −29 ‰ is illustrated by the black line, according to Fig. 1B. The maximum (MAX), minimum (MIN), average (AVG) and standard deviation (STDV) values are listed below each group. Analysis of variance (ANOVA) was performed on each data set, with p values listed at the bottom.

There is no evidence of hydrothermal fluid deposition of graphite in the DST chert nodules, excluding this as a cause of ultrastructural heterogeneity in the carbonaceous matter. Furthermore, the organic matter in the DST chert nodules has been homogeneously embedded in silica during pervasively mineralization, thereby eliminating mineral templating effects (cf. Van Zuilen et al., 2012) as a source of μm-scale structural heterogeneities. Lastly, as the Raman spectra were obtained by focusing the laser beam through the mineral onto organic matter in the subsurface, thin-section polishing artifacts (Beyssac et al., 2003; Ammar and Rouzaud, 2012; Maslova et al., 2012) cannot be the reason for the μm-scale structural heterogeneities.

After excluding the above possibilities, it is clear that the ultrastructural heterogeneities in the organic matter of the DST chert nodules reflect differences in the precursors of the carbonaceous material. In several previous studies, structural heterogeneities measured by Raman spectroscopy were also observed in organic matter in silicified microfossils, stromatolites, fungi, and plant fossils. These heterogeneities were attributed to differences in the carbon precursors of various subcellular components or co-existing organisms (Foucher et al., 2015; Qu et al., 2015). Their interpretations are also supported by fossilization experiments, where different species of microorganisms with dissimilar organic compounds (especially those in membranes) show different behaviors during silicification, giving rise to heterogeneities in "fossilized" organic matter (Orange et al., 2009).

5.2. Micro-FTIR data reflecting small-scale chemical heterogeneities in organic matter

The $R_{3/2}$ values of the organic matter in the center of nodules shows a bimodal distribution with modes at 0.12–0.16 and 0.48–0.73, respectively (Fig. 4B). The extremely low $R_{3/2}$ values suggest a contribution of long-chain organic carbon probably derived from eukaryotic remains (Igisu et al., 2009). This is consistent with previous reports of eukaryotic microfossils such as acanthomorphic acritarchs found in the center of DST chert nodules (Xiao, 2004; Yin et al., 2004; Muscente et al., 2015). On the other hand, organic matter with higher $R_{3/2}$ values (up to 0.73, Fig. 4B, Fig. 6A) in the center of DST nodules indicates the presence of branched carbon chains probably originating from prokaryotic biomass (Igisu

et al., 2009). Thus, the heterogeneous $R_{3/2}$ values indicate highly localized microbial communities in the center of chert nodules.

There are also differences in $R_{3/2}$ values among nodule center, nodule rim, and host rock (Fig. 4B). An ANOVA was performed on these three groups of measured $R_{3/2}$ values, giving a p value of 5×10^{-9} which indicates significant statistic differences among the nodule center, nodule rim, and host rock (Fig. 4B). The $R_{3/2}$ values of organic matter in the rim of DST nodules have a greater range (0.43–0.90) and a higher average (0.66) than those of the center and host rock (Fig. 4B and Fig. 6), indicating a predominance of highly branched carbon molecules in the nodule rim, possibly derived from bacterial or archaeal microbes. This is consistent with the model of chert nodule formation proposed by Xiao et al. (2010), where SRB were most abundant in the cortex and rim of the chert nodules. The organic matter in the host rock has intermediate $R_{3/2}$ values with a narrower range (from 0.34 to 0.64, Fig. 4B), probably because of better homogenization and mixing of organic matter due to microbial recycling and diagenetic compaction as the host rock was lithified much later than the nodules (Xiao et al., 2010).

5.3. The $\delta^{13}C$ variations in the organic matter

The range of $\delta^{13}C_{org\text{-}SIMS}$ data from −63.1 to −18.5‰ (Fig. 4C) encompasses the bulk $\delta^{13}C_{org}$ value of −29‰ (Fig. 1B, McFadden et al., 2008). Therefore, the $\delta^{13}C_{org\text{-}SIMS}$ data are not inconsistent with the bulk $\delta^{13}C_{org}$ data, but indicate much greater μm-scale variations that were previously unappreciated. This isotopic heterogeneity echoes structural and chemical heterogeneities as revealed by the Raman and FTIR data described above. The large range of $\delta^{13}C_{org\text{-}SIMS}$, which is up to 44‰ (apparent values from −63.1 to −18.5‰, Fig. 4C, Fig. 7), indicates multiple sources of the organic material produced by various microbes in the water column and sediments. Comparable μm-scale organic carbon isotope heterogeneities of up to 60‰ have been observed in modern symbiotic consortia of anaerobic methanotrophic archaea and sulfate reducing bacteria that are common in organic-rich anoxic marine sediments (Orphan et al., 2001, 2002; House et al., 2011).

Organic matter in the center and rim of the nodules has large isotopic range estimated to be up to 28‰ and 31‰, respectively (Fig. 4C), revealing dissimilar carbon precursors produced by different microbes (e.g., photoautotrophs and chemotrophs) using
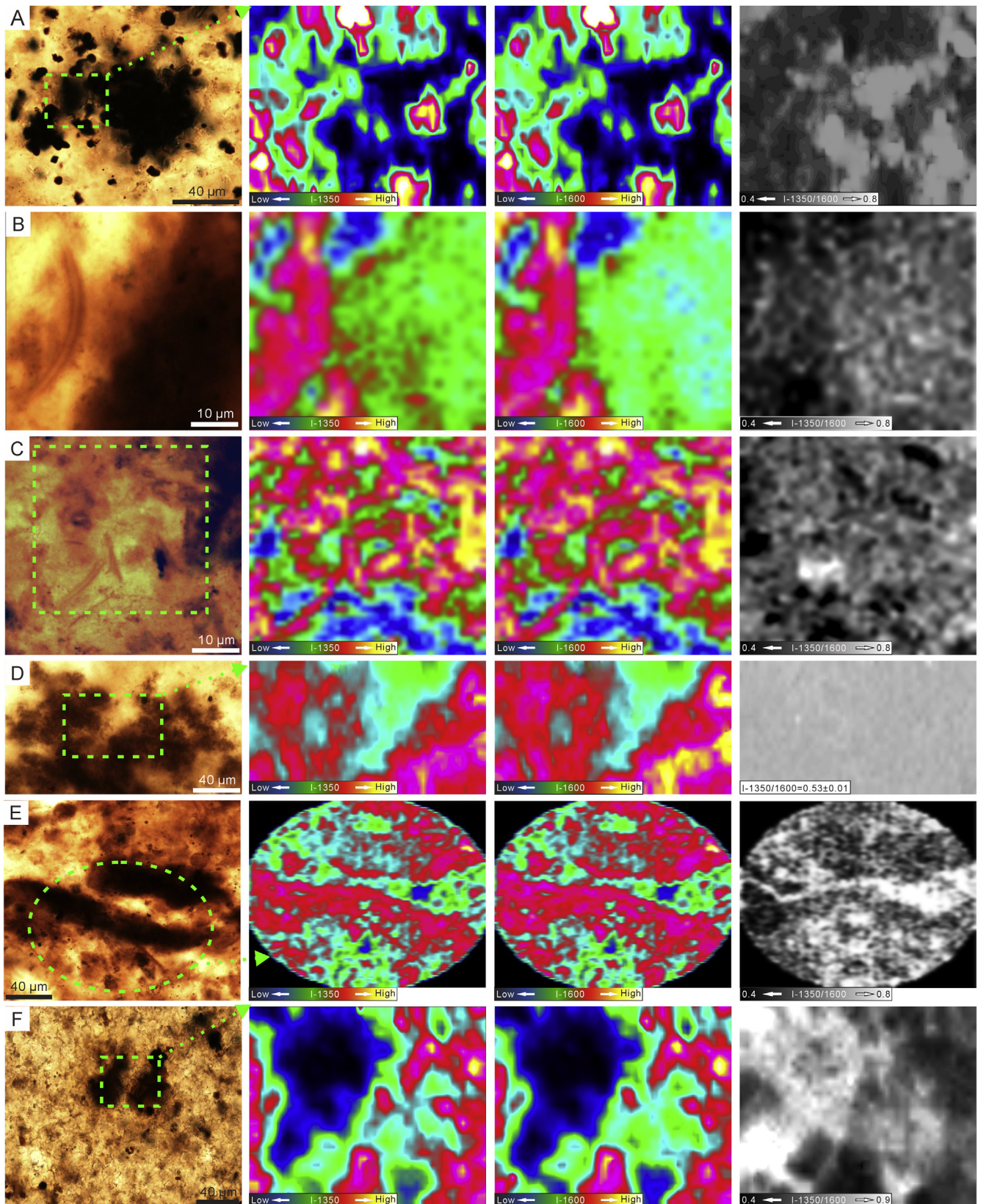
Fig. 5. Optical petrographic images and corresponding Raman maps showing spatial distribution and μm-scale ultrastructural heterogeneities of organic matter in DST nodules. Green dashed boxes and arrows denote location of Raman maps. Intensities of the 1350 and 1600 cm^{-1} bands are defined as I-1350 and I-1600, respectively, and intensity ratio of 1350 vs. 1600 cm^{-1} bands is defined as I-1350/1600. (A)–(D) Organic matter and filamentous microfossils in nodule center. (E) Organic matter in nodule rim. (F) Organic matter in the host rock. (For interpretation of the references to colour in this figure legend, the reader is referred to the web version of this article.)
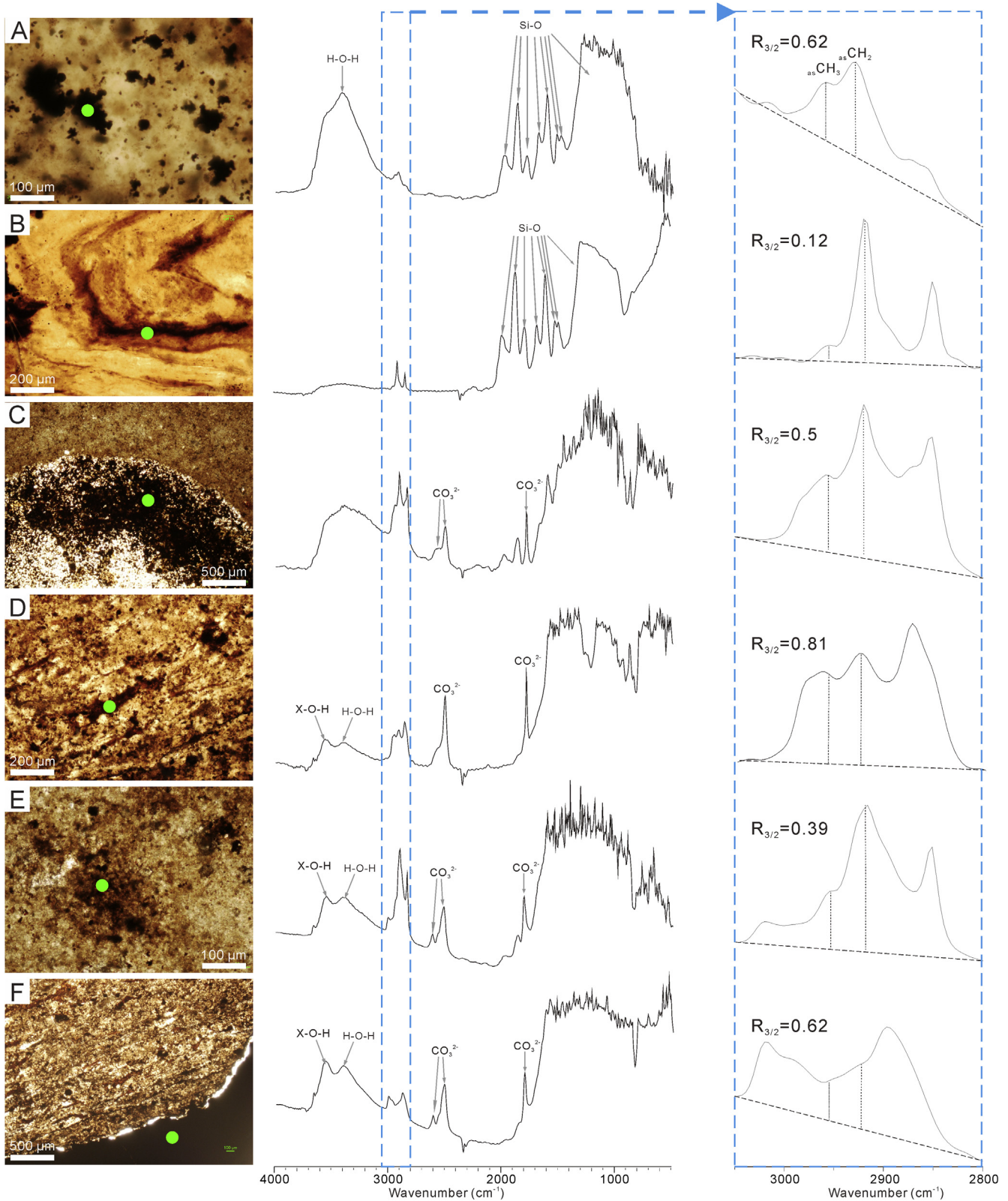
Fig. 6. IR spectra of organic matter in chert nodules, with analyzed locations marked by green dots in optical petrographic images. Blue dashed box on the left and arrow show the portion of IR spectra between 2800 to 3050 cm^{-1} that is enlarged on the right. (A) and (B) Organic matter and laminae in nodule center. (C) and (D) Organic matter and microbial mat fragments in nodule rim. (E) and (F) Organic matter in host rock. (For interpretation of the references to colour in this figure legend, the reader is referred to the web version of this article.)

different metabolic pathways. This is further supported by the pronounced chemical and ultrastructural heterogeneities recorded in the large range of $R_{3/2}$ and I-1350/1600 values (Figs. 4A and B, 5, and 6), which reflect various organic compounds with different branching index and molecular structural order from co-existing eukaryotic and prokaryotic biomass. An ANOVA
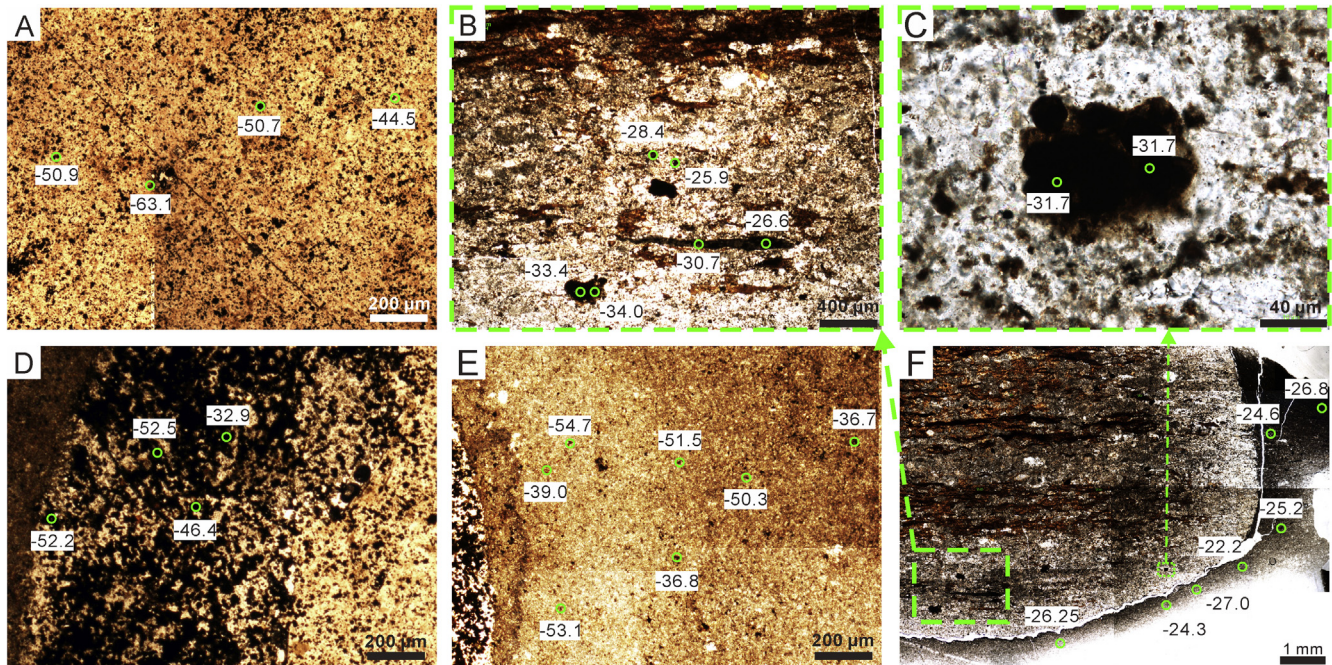
Fig. 7. Optical petrographic images showing locations of SIMS analyses (green circles) and SIMS $\delta^{13}C_{org}$ values (in ‰ V-PDB). (A) Organic matter in nodule center. (B)–(D) Organic matter in nodule rim. (E) and (F) Organic matter in host rock. Green boxes and arrows indicate enlarged areas. (For interpretation of the references to colour in this figure legend, the reader is referred to the web version of this article.)

shows statistic difference of $\delta^{13}C_{org\text{-}SIMS}$ values among the nodule center, rim and host rock (p = 0.015, Fig. 4C).

Indeed, the nodule center and rim have the lowest $\delta^{13}C_{org\text{-}SIMS}$ values (−63.1 and −56.7‰, respectively, Fig. 4C), indicating significant proportion of chemotrophic biomass, which is consistent with their maximum $R_{3/2}$ values (0.73 and 0.90 respectively, Fig. 4B). However, higher $\delta^{13}C_{org\text{-}SIMS}$ values also occur in the nodule center and rim (−35.1 and −26.6‰, respectively, Fig. 4C), due to the presence of eukaryotic photoautotrophs in the primary biomass, which would have relatively lower $R_{3/2}$ values (Fig. 4B). The organic matter in the host rock has the highest $\delta^{13}C_{org\text{-}SIMS}$ values (up to −18.5‰, Fig. 4C), probably indicating a smaller proportion of ^{13}C-depleted prokaryotic chemotrophic biomass. This would predict lower $R_{3/2}$ values in the host rock. Indeed, if one disregards the lower mode of the bimodal distribution of $R_{3/2}$ values of nodule center, there seems to be a decreasing pattern of average $R_{3/2}$ values going from nodule center to nodule rim to host rock, whereas average $\delta^{13}C_{org\text{-}SIMS}$ shows a corresponding increase (Fig. 4B, C). An important caveat, however, is that some of the heterogeneities may be due to the matrix effect as the nodule center, nodule rim, and host rock have different mineralogical and lithological compositions, and this effect is difficult to quantify.

5.4. Heterogeneous organic matter and its diverse origins

The DST chert nodules preserve a wide range of microfossils, including filamentous bacteria, multicellular algae, and acanthomorphic acritarchs (Xiao, 2004; Xiao et al., 2010; Yin et al., 2004, 2007; McFadden et al., 2008, 2009; Liu et al., 2014; Muscente et al., 2015), most of which likely represent phytoplankton in the water column and benthic microorganisms in microbial mats. These microfossils indicate that a diverse range of organisms, including eukaryotic and prokaryotic photoautotrophs, must have contributed to sedimentary organic carbon in the sediments. These organic remains could have provided carbon compounds to fuel additional microbial metabolic activities in the sediments, although these microbes may have not been preserved as body fossils.

Indeed, a SIMS-based study of pyrite sulfur isotopes in the rims of DST chert nodules suggests a significant role of bacterial sulfate reduction that created a micro-environment where fossil silicification and nodule formation was facilitated (Xiao et al., 2010). In addition to sulfate reduction bacteria, the large $\delta^{13}C_{org\text{-}SIMS}$ range and relatively low $\delta^{13}C_{org\text{-}SIMS}$ values in the chert nodules also indicate the possible presence of methanogens and methanotrophs. These microbes could have produced a complex microcosm in the sediments, accounting for the structural, chemical, and isotopic heterogeneities of organic matter preserved in the chert nodules.

In summary, the petrographic, I-1350/1600, $R_{3/2}$, and $^{13}C_{org\text{-}SIMS}$ data provide additional support for the models of chert nodule formation proposed by previous researchers (Xiao et al., 2010; Shen et al., 2011; Muscente et al., 2015) and reinforce the role of microbial activities in nodule formation and fossil preservation. The data also provide a more detailed view of structural, chemical, and isotopic heterogeneities of organic matter in DST chert nodules, and offer specific evidence for the contribution of eukaryotic and prokaryotic photoautotrophs, SRB, methanogens, and methanotrophs to carbonaceous material preserved in DST chert nodules and host rocks.

5.5. Implications for Ediacaran carbon cycles

One of the most remarkable features of Neoproterozoic carbon isotope record is the significant variations in both $\delta^{13}C_{carb}$ and $\delta^{13}C_{org}$ values, which are sometimes decoupled from each other (Rothman et al., 2003). The decoupled variations in $\delta^{13}C_{carb}$ and $\delta^{13}C_{org}$ are taken as evidence for the existence of an exceptionally large reservoir of dissolved organic carbon (DOC), which buffers the $\delta^{13}C_{org}$ record but can cause perturbations in the $\delta^{13}C_{carb}$ record if the DOC reservoir is partially oxidized (Fike et al., 2006; McFadden et al., 2008; Jiang et al., 2012). For example, the remarkably consistent and invariable $\delta^{13}C_{org}$ in Member II of the DST at the Jiulongwan section (Fig. 1B) was attributed to a large and isotopically buffered DOC reservoir, the more variable $\delta^{13}C_{org}$ values in Member III was interpreted as evidence for partial oxidation of

the DOC reservoir, and the negative $\delta^{13}C_{org}$ shift in Member IV as evidence for more extensive oxidation of the DOC reservoir and the assimilation of ^{13}C-depleted DIC in primary production (McFadden et al., 2008).

A premise of these interpretations is that the $\delta^{13}C_{org}$ values, measured from bulk sample total organic carbon (TOC), reflect the isotopic composition of an isotopically homogenous DOC reservoir. This premise is challenged by the new $\delta^{13}C_{org\text{-}SIMS}$ data presented here, which show significant μm-scale variations. Clearly, bulk sample $\delta^{13}C_{org}$ values do not necessarily record the carbon isotopic compositions of either primary production or oceanic DOC, because multiple groups of microorganisms can modify the isotopic signatures of TOC preserved in the sedimentary record. Furthermore, bulk sample $\delta^{13}C_{org}$ values, which record the weighted mean of all the different contributing organic compounds with various carbon isotopic compositions, do not reflect the heterogeneous isotopic characteristics of co-existing microbial consortia. For example, $\delta^{13}C$ values of individual organic compounds show marked deviation (up to 11‰) from those of total biomass of modern microbial mats consisting of photoautotrophs (Jahnke et al., 2004). In microbial ecosystems where carbon is cycled by chemotrophs, $\delta^{13}C$ of some lipid compounds, for instance fatty acids derived from SRB, could be distinctively lower than the $\delta^{13}C$ of the total biomass by as much as 17‰ (Londry et al., 2004). Even larger (>70‰) differences between compound-specific $\delta^{13}C$ values of chemotrophs and the $\delta^{13}C$ of total biomass have been reported in sediments near methane seeps (e.g. Hinrichs et al., 1999). Moreover, the $\delta^{13}C$ values of certain specific compounds derived from different chemotrophs could vary in cm-size, due to variations of their original microbial consortia and their associated microbial ecosystems in different depths of sediment (e.g. Elvert et al., 2005).

Concerning the DST chert nodules investigated here, a new picture emerges from the μm-scale heterogeneity in $\delta^{13}C_{org\text{-}SIMS}$ values, as opposed to the homogenous $\delta^{13}C_{org\text{-}bulk}$ values around -29‰. We suggest that this implies a predominantly photoautotrophic primary biomass with $\delta^{13}C$ value around -29‰, but co-existing chemotrophic microbes may have also contributed to TOC preserved in the Doushantuo Formation. The heterogeneous sources of organic carbon explain the μm-scale heterogeneity in I-1350/1600, $R_{3/2}$ and $\delta^{13}C$ values, but such heterogeneity is better preserved in early-lithified chert nodules than in highly compacted host rocks (argillaceous dolostone and mudstone), and can only be detected using analytical tools with a high spatial resolution. The observation that diverse microbial successions can modify the carbon isotopic signature preserved in the rock record has been reported in previous studies. For example, Qu et al. (2012), have shown that methanotrophs played a significant role in modulating a large negative $\delta^{13}C_{org}$ excursion in the Paleoproterozoic strata. Methanogens can also have a significant impact on the $\delta^{13}C_{carb}$ record, because they can preferentially reduce ^{13}C-depleted CO_2 in the pore water, leading to ^{13}C-enrichment in residual DIC and the formation of ^{13}C-enriched authigenic carbonates. Conversely, the anaerobic oxidation of methane can generate ^{13}C-depleted DIC and carbonate minerals. In combination, these microbial processes can produce highly complex and spatially heterogeneous carbon isotopic records in carbonate (Irwin et al., 1977; Boehme et al., 1996; Peckmann et al., 1999, 2002). This complexity in both $\delta^{13}C_{org}$ and $\delta^{13}C_{carb}$ can be disentangled only through in-situ analyses such as SIMS as done in this study.

6. Conclusions

Organic matter preserved in the chert nodules and host rock from the lower DST records μm-scale structural, chemical, and isotopic heterogeneities as measured in the Raman spectral parameter I-1350/1600 (ranging from 0.49 to 0.88), the infrared spectral index $R_{3/2}$ (ranging from 0.12 to 0.90), and $\delta^{13}C_{org\text{-}SIMS}$ (apparent values ranging from -63.1 to -18.5‰, V-PDB). These heterogeneities indicate diverse sources of organic carbon derived from chemotrophs including sulfate reducing bacteria, fermentation microorganisms such as methanogens, methanotrophs, as well as eukaryotic and prokaryotic photoautotrophs. The combination of in-situ techniques employed here reveals a complex assemblage of microorganisms that may have contributed to the organic carbon preserved in the DST, which are not discernable from paleontological data or bulk isotopic measurements. This study highlights the importance of diverse microbial activities in the Ediacaran marine ecosystem, and their potential role in chert nodule formation and exceptional fossil preservation via silicification (Xiao et al., 2010). Our findings also suggest that bulk sample $\delta^{13}C_{org}$ and $\delta^{13}C_{carb}$ values of Ediacaran rocks do not necessarily reflect the isotopic compositions of the DOC and DIC reservoirs in Ediacaran oceans, because various microbial processes in the sediments likely played important roles in modifying and contributing to the $\delta^{13}C_{org}$ and $\delta^{13}C_{carb}$ records. The μm-scale structural, chemical and isotopic heterogeneities of organic matter preserved in these DST chert nodules and their host rocks is a testament of these microbial processes.

Appendix A. Supplementary data

Supplementary data associated with this article can be found, in the online version, at http://dx.doi.org/10.1016/j.precamres.2017.01.003.

References

Aines, R.D., Rossman, G.R., 1984. Water in minerals – a peak in the infrared. J. Geophys. Res. 89, 4059–4071.

Ammar, M.R., Rouzaud, J.N., 2012. How to obtain a reliable structural characterization of polished graphitized carbons by Raman microspectroscopy. J. Raman Spectrosc. 43, 207–211.

Aoya, M., Kouketsu, Y., Endo, S., Shimizu, H., Mizukami, T., Nakamura, D., Wallis, S., 2010. Extending the applicability of the Raman carbonaceous-material geothermometer using data from contact metamorphic rocks. J. Metamorph. Geol. 28, 895–914.

Bailey, J.V., Corsetti, F.A., Greene, S.E., Crosby, C.H., Liu, P., Orphan, V.J., 2013. Filamentous sulfur bacteria preserved in modern and ancient phosphatic sediments: implications for the role of oxygen and bacteria in phosphogenesis. Geobiology 11, 397–405.

Bellamy, L., 1954. The Infra-Red Spectral of Complex Molecules. John Wiley & Sons, New York, pp. 13–56.

Bernard, S., Beyssac, O., Benzerara, K., Findling, N., Tzvetkov, G., Brown Jr., G.E., 2010. XANES, Raman and XRD study of anthracene-based cokes and saccharose-based chars submitted to high-temperature pyrolysis. Carbon 48, 2506–2516.

Beyssac, O., Goffé, B., Chopin, C., Rouzaud, J.N., 2002. Raman spectra of carbonaceous material in metasediments: a new geothermometer. J. Metamorph. Geol. 20, 859–871.

Beyssac, O., Goffé, B., Petitet, J., Froigneux, E., Moreau, M., Rouzaud, J.N., 2003. On the characterization of disordered and heterogeneous carbonaceous materials by Raman spectroscopy. Spectrochim Acta Part A 59, 2267–2276.

Boehme, S.E., Blair, N.E., Chanton, J.P., Martens, C.S., 1996. A mass balance of ^{13}C and ^{12}C in an organic-rich methane-producing marine sediment. Geochim. Cosmochim. Acta 60, 3835–3848.

Bonal, L., Quirico, E., Bourot-Denise, M., Montagnac, G., 2006. Determination of the petrologic type of CV3 chondrites by Raman spectroscopy of included organic matter. Geochim. Cosmochim. Acta 70, 1849–1863.

Bustin, R.M., Ross, J.V., Rouzaud, J.N., 1995. Mechanisms of graphite formation from kerogen: experimental evidence. Int. J. Coal Geol. 28, 1–36.

Chen, J.Y., Bottjer, D.J., Oliveri, P., Dornbos, S.Q., Gao, F., Ruffins, S., Chi, H.M., Li, C.W., Davidson, E.H., 2004. Small bilaterian fossils from 40 to 55 million years before the Cambrian. Science 305, 218–222.

Chen, J.Y., Bottjer, D.J., Li, G., Hadfield, M.G., Gao, F., Cameron, A.R., Zhang, C.Y., Xian, D.C., Tafforeau, P., Liao, X., Yin, Z.J., 2009. Complex embryos displaying bilaterian characters from Precambrian Doushantuo phosphate deposits, Weng'an, Guizhou. China. Proc. Natl. Acad. Sci. USA 106, 19056–19060.

Condon, D., Zhu, M., Bowring, S., Wang, W., Yang, A., Jin, Y., 2005. U-Pb ages from the neoproterozoic Doushantuo Formation, China. Science 308, 95–98.

Drake, H., Åström, M.E., Heim, C., Broman, C., Åström, J., Whitehouse, M., Ivarsson, M., Siljeström, S., Sjövall, P., 2015. Extreme 13C depletion of carbonates formed during oxidation of biogenic methane in fractured granite. Nat. Commun. 6. http://dx.doi.org/10.1038/ncomms8020. Article no. 7020.

Elvert, M., Hopmans, E., Treude, T., Boetius, A., Suess, E., 2005. Spatial variations of methanotrophic consortia at cold methane seeps: implications from a high-resolution molecular and isotopic approach. Geobiology 3, 195–209.

Fan, H.F., Zhu, X.K., Wen, H.J., Yan, B., Li, J., Feng, L.J., 2014. Oxygenation of Ediacaran Ocean recorded by iron isotopes. Geochim. Cosmochim. Acta 140, 80–94.

Fike, D.A., Grotzinger, J.P., Pratt, L.M., Summons, R.E., 2006. Oxidation of the Ediacaran Ocean. Nature 444, 744–747.

Foucher, F., Ammar, M.R., Westall, F., 2015. Revealing the biotic origin of silicified Precambrian carbonaceous microstructures using Raman spectroscopic mapping, a potential method for the detection of microfossils on Mars. J. Raman Spectrosc. 46, 873–879.

Franklin, R.E., 1951. Crystallite growth in graphitizing and non-graphitizing carbons. Proc. R. Soc. London Ser. A 209, 196–218.

Galvez, M.E., Beyssac, O., Martinez, I., Benzerara, K., Chaduteau, C., Malvoisin, B., Malavieille, J., 2013. Graphite formation by carbonate reduction during subduction. Nat. Geosci. 6, 473–477.

Grotzinger, J.P., Fike, D.A., Fischer, W.W., 2011. Enigmatic origin of the largest-known carbon isotope excursion in Earth's history. Nat. Geosci. 4, 285–292.

Guo, Q.J., Liu, C.Q., Strauss, H., Goldberg, T., Zhu, M.Y., Pi, D.H., Wang, J., 2006. Organic carbon isotope geochemistry of the Neoproterozoic Doushantuo Formation, South China. Acta Geol. Sin. (Engl. Ed.) 80, 670–683.

Hagadorn, J.W., Xiao, S.H., Donoghue, P.C.J., Bengtson, S., Gostling, N.J., Pawlowska, M., Raff, E.C., Raff, R.A., Turner, F.R., Chongyu, Y., Zhou, C., Yuan, X., McFeely, M.B., Stampanoni, M., Nealson, K.H., 2006. Cellular and subcellular structure of neoproterozoic animal embryos. Science 314, 291–294.

Hinrichs, K.-U., Hayes, J.M., Sylva, S.P., Brewer, P.G., DeLong, E.F., 1999. Methane-consuming archaebacteria in marine sediments. Nature 398, 802–805.

House, C.H., Schopf, J.W., Stetter, K.O., 2003. Carbon isotopic fractionation by Archaeans and other thermophilic prokaryotes. Org. Geochem. 34, 345–356.

House, C.H., Beal, E.J., Orphan, V.J., 2011. The apparent involvement of ANMEs in mineral dependent methane oxidation, as an analog for possible Martian methanotrophy. Life 1, 19–33.

House, C., Oehler, D., Sugitani, K., Mimura, K., 2013. Carbon isotopic analyses of c. 3.0 Ga microstructures imply planktonic autotrophs inhabited Earth's early oceans. Geology 41, 651–654.

Igisu, M., Nakashima, S., Ueno, Y., Awramik, S.M., Maruyama, S., 2006. *In Situ* Infrared microspectroscopy of 850 million-year-old prokaryotic fossils. Appl. Spectrosc. 60, 1111–1120.

Igisu, M., Ueno, Y., Shimojima, M., Nakashima, S., Awramik, S.M., Ohta, H., Maruyama, S., 2009. Micro-FTIR spectroscopic signatures of bacterial lipids in Proterozoic microfossils. Precambrian Res. 173, 19–26.

Igisu, M., Komiya, T., Kawashima, M., Nakashima, S., Ueno, Y., Han, J., Shu, D., Li, Y., Guo, J., Maruyama, S., 2014. FTIR microspectroscopy of Ediacaran phosphatized microfossils from the Doushantuo Formation, Weng'an, South China. Gondwana Res. 25, 1120–1138.

Irwin, H., Curtis, C., Coleman, M., 1977. Isotopic evidence for source of diagenetic carbonates formed during burial of organic-rich Sediments. Nature 269, 209–213.

Ito, Y., Nakashima, S., 2002. Water distribution in low-grade siliceous metamorphic rocks by micro-FTIR and its relation to grain size: a case from the Kanto Mountain region. Jpn. Chem. Geol. 189, 1–18.

Jahnke, L.L., Embaye, T., Hope, J., Turk, K.A., Van Zuilen, M., Des Marais, D.J., Farmer, J.D., Summons, R.E., 2004. Lipid biomarker and carbon isotopic signatures for stromatolite-forming, microbial mat communities and Phormidium cultures from Yellowstone National Park. Geobiology 2, 31–47.

Jiang, G.Q., Kaufman, A.J., Christie-Blick, N., Zhang, S.H., Wu, H.C., 2007. Carbon isotope variability across the Ediacaran Yangtze platform in South China: implications for a large surface-to-deep ocean $\delta^{13}C$ gradient. Earth Planet. Sci. Lett. 261, 303–320.

Jiang, G.Q., Wang, X.Q., Shi, X.Y., Zhan, S.H., Xiao, S.H., Dong, J., 2010. Organic carbon isotope constraints on the dissolved organic carbon (DOC) reservoir at the Cryogenian-Ediacaran transition. Earth Planet. Sci. Lett. 299, 159–168.

Jiang, G.Q., Shi, X.Y., Zhang, S.H., Wang, Y., Xiao, S.H., 2011. Stratigraphy and paleogeography of the Ediacaran Doushantuo Formation (ca. 635–551 Ma) in South China. Gondwana Res. 19, 831–849.

Jiang, G.Q., Wang, X.Q., Shi, X.Y., Xiao, S.H., Zhang, S.H., Dong, J., 2012. The origin of decoupled carbonate and organic carbon isotope signatures in the early Cambrian (ca. 542–520 Ma) Yangtze platform. Earth Planet. Sci. Lett. 317, 96–110.

Kaufman, A.J., Xiao, S., 2003. High CO_2 levels in the Proterozoic atmosphere estimated from analyses of individual microfossils. Nature 425, 279–282.

Kouketsu, Y., Mizukami, T., Mori, H., Endo, S., Aoya, M., Hara, H., Nakamura, D., Wallis, S., 2014. A new approach to develop the Raman carbonaceous material geothermometer for low-grade metamorphism using peak width. Isl. Arc 23, 33–50.

Lahfid, A., Beyssac, O., Deville, E., Negro, F., Chopin, C., Goffe, B., 2010. Evolution of the Raman spectrum of carbonaceous material in low-grade metasediments of the Glarus Alps (Switzerland). Terra Nova 22, 354–360.

Lepland, A., van Zuilen, M.A., Philippot, P., 2011. Fluid deposited graphite and its geobiological implications in early Archean gneiss from Akilia, Greenland. Geobiology 9, 2–9.

Lepot, K., Williford, K.H., Ushikubo, T., Sugitani, K., Mimura, K., Spicuzza, M.J., Valley, J.W., 2013. Texture-specific isotopic compositions in 3.4 Gyr old organic matter support selective preservation in cell-like structures. Geochim. Cosmochim. Acta 112, 66–86.

Li, C., Love, G.D., Lyons, T.W., Fike, D.A., Sessions, A.L., Chu, X.L., 2010. A stratified redox model for the Ediacaran Ocean. Science 328, 80–83.

Liu, P., Yin, C., Gao, L., Tang, F., Chen, S., 2009. New material of microfossils from the Ediacaran Doushantuo Formation in the Zhangcunping area, Yichang, Hubei Province and its zircon SHRIMP U-Pb age. Chin. Sci. Bull. 54, 1058–1064.

Liu, P., Xiao, S., Yin, C., Chen, S., Zhou, C., Li, M., 2014. Ediacaran acanthomorphic acritarchs and other microfossils from chert nodules of the upper Doushantuo Formation in the Yangtze Gorges area, South China. J. Paleontol. 88, 1–139.

Londry, K., Jahnke, L., Des Marais, D., 2004. Stable carbon isotope ratios of lipid biomarkers of sulfate-reducing bacteria. Appl. Environ. Microbiol. 70, 745–751.

Luque, F.J., Barrenechea, J.F., Millward, D., Beyssac, O., Huizenga, J., 2009. Deposition of highly crystalline graphite from moderate–temperature fluids. Geology 37, 275–278.

Marshall, C.P., Javaux, E.J., Knoll, A.H., Walter, M.R., 2005. Combined micro-Fourier transform infrared (FTIR) spectroscopy and micro-Raman spectroscopy of Proterozoic acritarchs: a new approach to Palaeobiology. Precambrian Res. 138, 208–224.

Maslova, O., Ammar, M., Guimbretière, G., Rouzaud, J.-N., Simon, P., 2012. Determination of crystallite size in polished graphitized carbon by Raman spectroscopy. Phys. Rev. B 86, 134205.

McFadden, K.A., Huang, J., Chu, X.L., Jiang, G.Q., Kaufman, A.J., Zhou, C.M., Yuan, X.L., Xiao, S.H., 2008. Pulsed oxidation and biological evolution in the Ediacaran Doushantuo Formation. Proc. Natl. Acad. Sci. USA 105, 3197–3202.

McFadden, K.A., Xiao, S.H., Zhou, C.M., Kowalewski, M., 2009. Quantitative evaluation of the biostratigraphic distribution of acanthomorphic acritarchs in the Ediacaran Doushantuo Formation in the Yangtze Gorges area, South China. Precambrian Res. 173, 170–190.

Muscente, A., Hawkins, A.D., Xiao, S., 2015. Fossil preservation through phosphatization and silicification in the Ediacaran Doushantuo Formation (South China): a comparative synthesis. Palaeogeogr. Palaeoclimatol. Palaeoecol. 434, 46–62.

Orange, F., Westall, F., Disnar, J.R., Prieur, D., Bienvenu, N., Le Romancer, M., Défarge, C., 2009. Experimental silicification of the extremophilic Archaea *Pyrococcus abyssi* and *Methanocaldococcus jannaschii*: applications in the search for evidence of life in early Earth and extraterrestrial rocks. Geobiology 7, 403–418.

Orphan, V.J., House, C.H., Hinrichs, K.U., McKeegan, K.D., DeLong, E.F., 2001. Methane–consuming archaea revealed by directly coupled isotopic and phylogenetic analysis. Science 293, 484–487.

Orphan, V.J., House, C.H., Hinrichs, K.U., McKeegan, K.D., DeLong, E.F., 2002. Multiple archaeal groups mediate methane oxidation in anoxic cold seep sediments. Proc. Natl. Acad. Sci. USA 99, 7663–7668.

Peckmann, J., Thiel, V., Michaelis, W., Clari, P., Gaillard, C., Martire, L., Reitner, J., 1999. Cold seep deposits of Beauvoisin (Oxfordian; southeastern France) and Marmorito (Miocene; northern Italy): microbially induced authigenic carbonates. Int. J. Earth. Sci. 88, 60–75.

Peckmann, J., Goedert, J.L., Thiel, V., Michaelis, W., Reitner, J., 2002. A comprehensive approach to the study of methane-seep deposits from the Lincoln Creek Formation, western Washington State, USA. Sedimentology 49, 855–873.

Qu, Y., Črne, A.E., Lepland, A., Van Zuilen, M.A., 2012. Methanotrophy in a paleoproterozoic oil field ecosystem, Zaonega Formation, Karelia, Russia. Geobiology 10, 467–478.

Qu, Y., Engdahl, A., Zhu, S., Vajda, V., McLoughlin, N., 2015. Ultrastructural heterogeneity of carbonaceous material in ancient cherts: investigating biosignature origin and preservation. Astrobiology 15, 825–842.

Rahl, J.M., Anderson, K.M., Brandon, M.T., Fassoulas, C., 2005. Raman spectroscopic carbonaceous material thermometry of low-grade metamorphic rocks: calibration and application to tectonic exhumation in Crete, Greece. Earth Planet. Sci. Lett. 240, 339–354.

Rividi, N., van Zuilen, M., Philippot, P., Ménez, B., Godard, G., Poidatz, E., 2010. Calibration of carbonate composition using micro–Raman analysis: application to planetary surface exploration. Astrobiology 10, 293–309.

Romero-Sarmiento, M.-F., Rouzaud, J.-N., Bernard, S., Deldicque, D., Thomas, M., Littke, R., 2014. Evolution of Barnett Shale organic carbon structure and nanostructure with increasing maturation. Org. Geochem. 71, 7–16.

Rothman, D.H., Hayes, J.M., Summons, R.E., 2003. Dynamics of the Neoproterozoic carbon cycle. Proc. Natl. Acad. Sci. USA 100, 8124–8129.

Sadezky, A., Muckenhuber, H., Grothe, H., Niessner, R., Pöschl, U., 2005. Raman microspectroscopy of soot and related carbonaceous materials: spectral analysis and structural information. Carbon 43, 1731–1742.

Schidlowski, M., 2001. Carbon isotopes as biogeochemical recorders of life over 3.8 Ga of Earth history: evolution of a concept. Precambrian Res. 106, 117–134.

Schiffbauer, J.D., Yin, L., Bodnar, R.J., Kaufman, A.J., Meng, F., Hu, J., Shen, B., Yuan, X., Bao, H., Xiao, S., 2007. Ultrastructural and geochemical characterization of Archean-Paleoproterozoic graphite particles: implications for recognizing traces of life in highly metamorphosed rocks. Astrobiology 7, 684–704.

Schiffbauer, J., Wallace, A., Hunter, J., Kowalewski, M., Bodnar, R., Xiao, S., 2012. Thermally-induced structural and chemical alteration of organic-walled microfossils: an experimental approach to understanding fossil preservation in metasediments. Geobiology 10, 402–423.

Sforna, M., van Zuilen, M., Philippot, P., 2014. Structural characterization by Raman hyperspectral mapping of organic carbon in the 3.46 billion-year-old Apex chert, Western Australia. Geochim. Cosmochim. Acta 124, 18–33.

Shen, B., Lee, C.T., Xiao, S.H., 2011. Germanium/silicon ratios of diagenetic chert nodules in the Ediacaran Doushantuo Formation, South China. Chem. Geol. 74. A945–A945.

Tahata, M., Ueno, Y., Ishikawa, T., Sawaki, Y., Murakami, K., Han, J., Shu, D., Li, Y., Guo, J., Yoshida, N., 2013. Carbon and oxygen isotope chemostratigraphies of the Yangtze platform, South China: decoding temperature and environmental changes through the Ediacaran. Gondwana Res. 23, 333–353.

Tuinstra, F., Koenig, J.L., 1970. Raman spectrum of graphite. J. Chem. Phys. 53, 1126.

van Zuilen, M.A., Fliegel, D., Wirth, R., Lepland, A., Qu, Y., Schreiber, A., Romashkin, A. E., Philippot, P., 2012. Mineral-templated growth of natural graphite films. Geochim. Cosmochim. Acta 83, 252–262.

Wen, H., Fan, H., Tian, S., Wang, Q., Hu, R., 2016. The formation conditions of the early Ediacaran cherts, South China. Chem. Geol. 430, 45–69.

Williford, K.H., Ushikubo, T., Schopf, J.W., Lepot, K., Kitajima, K., Valley, J.W., 2013. Preservation and detection of microstructural and taxonomic correlations in the carbon isotopic compositions of individual Precambrian microfossils. Geochim. Cosmochim. Acta 104, 165–182.

Wopenka, B., Pasteris, J.D., 1993. Structural characteristics of kerogens to granulite-facies graphite: applications of Raman microprobe spectroscopy. Am. Mineral. 78, 533–557.

Xiao, S.H., 2004. New multicellular algal fossils and acritarchs in Doushantuo chert nodules (Neoproterozoic; Yangtze Gorges, south China). J. Paleontol. 78, 393–401.

Xiao, S.H., Zhang, Y., Knoll, A.H., 1998. Three-dimensional preservation of algae and animal embryos in a Neoproterozoic phosphorite. Nature 391, 553–558.

Xiao, S.H., Hagadorn, J.W., Zhou, C.M., Yuan, X.L., 2007. Rare helical spheroidal fossils from the Doushantuo Lagerstatte: Ediacaran animal embryos come of age? Geology 35, 115–118.

Xiao, S.H., Schiffbauer, J.D., McFadden, K.A., Hunter, J., 2010. Petrographic and SIMS pyrite sulfur isotope analyses of Ediacaran chert nodules: implications for microbial processes in pyrite rim formation, silicification, and exceptional fossil preservation. Earth Planet. Sci. Lett. 297, 481–495.

Xiao, S.H., McFadden, K.A., Peek, S., Kaufman, A.J., Zhou, C.M., Jiang, G.Q., Hu, J., 2012. Integrated chemostratigraphy of the Doushantuo Formation at the northern Xiaofenghe section (Yangtze Gorges, South China) and its implication for Ediacaran stratigraphic correlation and ocean redox models. Precambrian Res. 192–95, 125–141.

Xiao, S., Muscente, A., Chen, L., Zhou, C., Schiffbauer, J.D., Wood, A.D., Polys, N.F., Yuan, X., 2014a. The Weng'an biota and the Ediacaran radiation of multicellular eukaryotes. Nat. Sci. Rev. 1, 498–520.

Xiao, S.H., Zhou, C.M., Liu, P.J., Wang, D., Yuan, X.L., 2014b. Phosphatized acanthomorphic acritarchs and related microfossils from the Ediacaran Doushantuo Formation at Weng'an (South China) and their implications for biostratigraphic correlation. J. Paleontol. 88, 1–67.

Yin, C., Bengtson, S., Yue, Z., 2004. Silicified and phosphatized Tianzhushania, spheroidal microfossils of possible animal origin from the Neoproterozoic of South China. Acta Palaeontol. Pol. 49, 1–12.

Yin, L.M., Zhu, M.Y., Knoll, A.H., Yuan, X.L., Zhang, J.M., Hu, J., 2007. Doushantuo embryos preserved inside diapause egg cysts. Nature 446, 661–663.

Zerkle, A.L., House, C.H., Brantley, S.L., 2005. Biogeochemical signatures through time as inferred from whole microbial genomes. Am. J. Sci. 305, 467–502.

Zhou, C., Xiao, S., 2007. Ediacaran δ^{13}C chemostratigraphy of South China. Chem. Geol. 237, 89–108.

Zhu, B., Becker, H., Jiang, S.-Y., Pi, D.–H., Fischer-Gödde, M., Yang, J.–H., 2013. Re-Os geochronology of black shales from the Neoproterozoic Doushantuo Formation, Yangtze platform, South China. Precambrian Res. 225, 67–76.